Generation of dissipative Kerr solitons in a passive fiber Kerr resonator with a fast saturable absorber

Fan Yang [1], Zhiqiang Wang [2,3,*] and Zuxing Zhang [1]

[1] *College of Electronic and Optical Engineering & College of Flexible Electronics (Future Technology), Nanjing University of Posts and Telecommunications, Nanjing 210003, China*

[2] *The Information Materials and Intelligent Sensing Laboratory of Anhui Province, Anhui University, Hefei 230039, China*

[3] *Aston Institute of Photonic Technologies, Aston University, Birmingham B4 7ET, United Kingdom*

(Received 30 June 2022; revised 15 November 2022; accepted 10 January 2023; published 31 January 2023)

The generation of dissipative Kerr solitons (DKSs) in a passive fiber Kerr resonator with a fast saturable absorber (SA) is studied numerically. Simulation results demonstrate the generation of DKSs in SA-based fiber Kerr resonators. The impact of the properties of an SA, including the modulation depth and the saturation power, on the performances of DKSs is studied. Our results show the existence of DKSs in SA-based passive fiber Kerr resonators, suggesting that the SA provides additional degrees of freedom to get access to the DKS regime in Kerr resonators in addition to the detuning and the pump. These findings provide guidance for the experimental realization of the generation of DKSs in SA-based fiber Kerr resonators.

DOI: 10.1103/PhysRevA.107.013530

I. INTRODUCTION

Passive Kerr resonators as dissipative systems support many different localized solutions, among which the temporal dissipative Kerr soliton (DKS) has received the most attention in the past two decades. DKSs are stable ultrashort pulses featuring excellent low noise [1,2], and they manifest as equally spaced frequency combs in the frequency domain. The demonstration of a DKS in a passive fiber resonator [1] followed by the realization of the DKS in chip-scale microresonators [3] has fully released the potential of the DKS for many applications. As a Kerr frequency comb, it has already been successfully used in a wide range of applications, such as optical communications [4], optical synthesizers [5], optical clocks [6], LIDAR (light detection and ranging) [7], spectrometers [8], and microwave photonics [9].

In Kerr resonators, the DKS is a result of the balance between dispersion and nonlinearity on the one hand, and between parametric gain and loss on the other [3]. The latter is particularly important. In coherently driven Kerr resonators, a process of four-wave mixing (FWM) [10] occurs when the pump power reaches the threshold of modulation instabilities (MIs) in the cavity [11]. The FWM process leads to the generation of two sidelobes symmetrically sitting on both sides of the pump frequency in the spectrum. Further increasing the pump power leads to a cascaded FWM process [12], resulting in a transition of the intracavity field to an MI-induced Turing pattern or DKS state. The DKS is usually formed in the red-detuned region where the system is intrinsically thermally unstable. Therefore, the challenge of getting a stable DKS in practice is to overcome the thermal effects. In experiments, a method called detuning scan is a universal technique to get DKSs in Kerr resonators [3]. The detuning that is defined as the frequency offset between the pump frequency and the cavity resonance is the key parameter to get the DKS. A delicate adjustment of the detuning scan speed and accuracy overcomes the variation of the resonant frequency due to the thermal effect [13,14], thus enabling one to lock the pump frequency to the cavity resonance in the detuning scan process. Via scanning the detuning from the blue-detuned to the red-detuned region, the phase of all modes can be locked under certain detuning [15]. Consequently, a phase-locked state of the DKS is observed. Other similar methods, including the forward and backward detuning scan [16], power-kicking [17], auxiliary-laser-based thermal controlling [18], and heat management [19], are proposed and have been demonstrated to excite DKSs in microresonators successfully.

One prominent issue of DKSs in Kerr resonators is the lower energy transfer efficiency from the narrow continuous wave (CW) pump to the intracavity field due to the small fraction of the overlapping of the CW with the intracavity field [19,20]. Because of this, DKS has lower single-pulse energy (typically dozens of pJ). Approaches such as dark solitons [21,22], pulse-pumping [23,24], and mutually coupled Kerr resonators [25] have been demonstrated to improve the utilization of the pump, and to improve the pump-soliton efficiency. Noticeably, in recent years the concepts of dispersion/nonlinearity management [26,27] and gain management [28] have been introduced into the field of Kerr resonators, enabling one to explore the rich nonlinear dynamics of DKSs and to get DKSs in Kerr resonators more efficiently. This boosts the performances of the DKS in terms of the pulse duration and energy, though the state-of-the-art pulse energy of the DKS is still far below the nJ level, which is much lower than its counterparts of solitons from mode-locked lasers [29,30].

Apart from the lower energy, another main outstanding challenge confronting the field of Kerr micro/fiber resonators

*Corresponding author: ewangzhiqiang1987@hotmail.com

is developing reliable and repeatable approaches to achieve the stable operation of Kerr solitons, particularly a single soliton state. The critical and strict conditions that are required to initiate and maintain soliton states against perturbations increase the system's complexity and also its susceptibility to perturbations. This is especially evident in fiber Kerr resonators. The spontaneous emergence of stable Kerr solitons in fiber Kerr resonators is usually difficult to achieve, and the excitation of Kerr solitons often requires additional proper perturbation of system variables, for instance using a writing pulse, phase/intensity modulation of the pump light, and mechanically perturbing the cavity by shaking the fibers [31–33]. People are keen to find an effective way to realize the self-starting and robust operation of Kerr solitons in fiber Kerr resonators.

Remarkably, recent literature shows that the transient loss modulation introduced by saturable absorbers (SAs) is an effective way to generate DKSs with high robustness and pump-soliton efficiency in microresonators when achieving the DKS state on resonance [34,35]. The SA is an optical component with nonlinear absorption of light. Specifically, the SA absorption is high for low-intensity light and is reduced significantly for high-intensity light. One of the main applications of an SA is to initiate the mode-locking of lasers for the generation of short pulses. The SA enhances the fluctuations emitted from the spontaneous emission inside a laser cavity during multiple roundtrips until one intensive pulse is selected and an ultrashort pulse is formed. One could expect that an SA in fiber Kerr resonators could overcome the pain points of the spontaneous generation and the robustness of the DKS operation in such a system. This is the strong motivation behind this work.

When dealing with ultrafast fiber lasers, artificial fast SAs are the most widely used devices for getting ultrashort pulses. These SAs take several forms, based on different configurations, such as nonlinear polarization rotation in a fiber, a nonlinear fiber loop mirror, and a nonlinear amplified loop mirror. Compared to slow SAs, ultrafast lasers with fast SAs usually yield shorter pulses due to the rapid recovery time, which is well below the pulse duration. Thinking from the perspective of the simple structure, easier integration, and ultrashort pulse generation, in this work we focus on studying the DKS generation in a fiber Kerr resonator with a fast SA.

In this article, we have studied the generation of a DKS in a fiber Kerr resonator with a fast SA in the cavity. The SA provides a power-dependent transmission function in the cavity to reshape and stabilize the pulses. Simulation results of the Ikeda map reveal the DKS formation in the SA-based fiber Kerr resonator. The parameter region for DKS formation in the SA-based fiber Kerr resonator is given in a two-dimensional space of (Δ, P). The impacts of the SA properties on the DKS performances are also studied. These results enrich our understanding of the nonlinear dynamics of DKSs and provide an ideal platform to realize the generation of DKSs in Kerr fiber resonators.

II. SIMULATION MODEL

The simulation model that we use is a pure passive optical fiber ring resonator with a fast SA inside the resonator. The

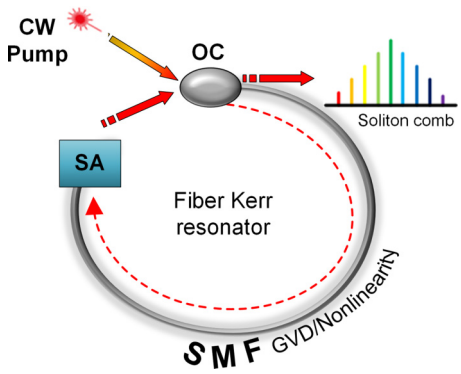

FIG. 1. Schematic diagram of the simulation model of the passive fiber Kerr resonator with a fast saturable absorber inside the cavity. SA denotes saturable absorber, OC denotes optical coupler, CW denotes continuous-wave light, SMF denotes single-mode fiber, and GVD denotes group velocity dispersion.

resonator consists of an 85-m-long single-mode fiber (SMF), which is coherently pumped by a CW laser through a 10:90 optical coupler. 10% of the intracavity light has been extracted for characterization. A schematic of the resonator is presented in Fig. 1. The behavior of such a system is governed by the so-called generalized Ikeda map. In simulations, the electric field propagating in the resonator follows a concatenated sequence representing different cavity elements. First, the field envelope $E_N(z,\tau)$ that stands for the time-domain electric light field inside the resonator at the Nth roundtrip traveling along the fiber in the cavity can be obtained by numerically solving a standard nonlinear Schrödinger equation,

$$\frac{\partial E_N(z,\tau)}{\partial z} = -i\frac{\beta_2}{2}\frac{\partial^2 E_N}{\partial \tau^2} + i\gamma|E_N|^2 E_N, \tag{1}$$

where β_2 is the group velocity dispersion (GVD) and γ is the nonlinearity coefficient. z is the longitudinal coordinate along the optical fiber, and τ denotes the time in the pulse group velocity reference frame. The subscript N stands for the Nth roundtrip.

After that, the electric light field $E_N(z=L,\tau)$ output from the fiber passes a fast SA in the resonator. L is the fiber length, namely the cavity roundtrip length. The SA in our model is modeled by an instantaneous loss function α_{SA}:

$$\alpha_{\mathrm{SA}}(\tau) = \frac{L_0}{1+|E(\tau)|^2/P_{\mathrm{sat}}}. \tag{2}$$

Here, L_0 is the modulation depth of the SA, $P(\tau)=|E(\tau)|^2$ being the instantaneous power. P_{sat} stands for the saturation power of the SA. Therefore, the electric field at the end of the Nth roundtrip can be obtained by multiplying the field envelope output from the fiber by the SA transfer function,

$$E'_N(z=L,\tau) = \sqrt{1-\alpha_{\mathrm{SA}}}E_N(z=L,\tau). \tag{3}$$

In transit from the Nth roundtrip to the $(N+1)$th roundtrip, the electric light field $E_{N+1}(z=0,\tau)$ obeys the following roundtrip transit condition:

$$E_{N+1}(z=0,\tau) = \sqrt{\theta}E_{\mathrm{in}} + \sqrt{1-\alpha}e^{-i\delta}E'_N(z=L,\tau), \tag{4}$$

where $E_{N+1}(z=0,\tau)$ stands for the intracavity electric light field at the beginning of the $(N+1)$th roundtrip. E_{in} is the driving field that is injected into the cavity superimposing on the intracavity field in each roundtrip. θ is the power transmission coefficient of the input optical coupler. δ denotes the phase detuning between the driving field and one cavity resonance. α stands for the total cavity loss per roundtrip, which includes all the component losses and fiber loss. All the numerical simulation results presented in our manuscript are obtained by solving Eqs. (1)–(4). In the rest of this article, we will use the term of a lumped model referring to Eqs. (1)–(4).

In the simulations, we solve Eq. (1) by using a distributed split-step Fourier transform method where the linear terms are solved in the frequency domain, whereas the nonlinear effect is integrated directly in the time domain using the fourth-order Runge-Kutta method. The time window is set to 100 ps and the grid point is 2048. The parameter of the fiber is chosen to match the typical experimental values: $\beta_2 = -20$ ps^2/km and $\gamma = 1.3$ w^{-1}/km at 1550 nm. The pump coupling ratio is 10%, and the total cavity roundtrip loss is $\alpha = 0.233$. The initial field condition is a random noise field.

III. SIMULATION RESULTS

In what follows, the numerical simulation results are presented in three sections. In the first section, we simulate the Ikeda map of our system for an SA with $L_0 = 0.08$ and $P_{\text{sat}} = 10$ W though solving the lumped model, confirming the existence of the DKS in such a system. Later on, a two-dimensional space of (Δ, F) (Δ is the detuning and F is the pump power) is introduced to divide the parameter plane into different regions, corresponding to different types of solutions. In the third section, the performances of DKSs for different SA properties are studied and discussed.

A. DKS formation in the SA-based fiber Kerr resonator

We start with the simulation of the Ikeda-map via the detuning scan technique, confirming the existence of the DKS in the SA-based fiber Kerr resonator. The pump power is 2.7 W and the SA has parameters of $L_0 = 0.08$ and $P_{\text{sat}} = 10$ W. Considering that the system is bistable and highly nonlinear, we notice that the final states for each parameter set are sensitive to the initial conditions. In Fig. 2 we present only one example of the Ikeda map of the evolution of the intracavity field with an initial condition of random noise with a peak power varying from 0 to 1 W. Figures 2(a) and 2(b) show the temporal and spectral evolution of the intracavity field, respectively. In the beginning, the resonator operates in the CW regime due to the imperfect phase matching between the pump frequency and the cavity resonance. Along with a further scan of the detuning from the blue-detuned to the red-detuned side, the power of the intracavity field increases. When the pump power reaches the MI threshold at $\delta = -0.08\pi$ rad, the system transits from the CW regime into a Turing roll pattern that is a state with evenly spaced combs in the spectral domain and periodic waveforms distributed within the cavity in the time domain [Figs. 2(e) and 2(f)]. Further sweeping the detuning from 0.08π rad into the red-detuned region leads to chaotic MI patterns, followed by the generation of breathing DKSs and multiple DKSs in a detuning range from 0.2π to 0.33π rad and then a stable single DKS within a range from 0.33π to 0.78π rad.

We also traced the energy of the intracavity field during the detuning scan process, revealing clear boundaries determining the region for different regimes. The energy is defined as the total energy of the optical light field in the cavity, namely the integral of its optical power over time. It can be expressed as $E_p = \int_{-T/2}^{T/2} |E|^2 dt$. T is the time window of 100 ps in simulations. Figure 2(c) depicts the evolution of the energy of the intracavity field at a pump power of 2.7 W, exhibiting a rapid drop in the energy at $\delta = 0.2\pi$ rad, which is an indication of the onset of the DKS step. One example of the DKS state at $\delta = 0.4\pi$ rad is presented in Figs. 2(g) and 2(h). The broad and smooth spectrum is centered at 1550 nm with a 3 dB width of 1.78 nm. The peak sitting atop the spectrum is the residual CW light. The symmetric sidebands on both sides of the spectrum are caused by periodic cavity loss. The pulse [blue curve in Fig. 2(h)] has a peak power of 23.83 W and a pulse width of 1.37 ps.

B. Map of different solutions in a two-dimensional space of (Δ, F)

In this section, we aim to find the existence region of the DKS in the SA-based fiber Kerr resonator in a two-dimensional map in the space of the detuning and pump power (Δ, F). Note that Δ and F are the normalized unitless detuning and pump power (see details of the normalization in Appendix A). In simulations, the detuning δ_0 is changing from 0 to 0.8π rad and the pump power P_{in} is varying from 0.5 to 2.9 W. Using the form of $F = \theta\gamma L P_{\text{in}}/\alpha^3$ and $\Delta = \delta_0/\alpha$, the normalized Δ is calculated to be within a range from 0 to 21.5, and F is from 3.5 to 20. Depending on the parameter set, various stationary solutions are observed, including the CW solutions (white area), the Turing roll pattern (not shown in Fig. 3), the chaotic pattern (light yellow punctate area), as well as breathers and DKS solutions (light blue area enclosed by stars). As we are more interested in the DKS state, only the region with a normalized detuning of $\Delta > 0$ is plotted in Fig. 3. Such a plot enables one to get insight into the DKS generation in an SA-based fiber Kerr resonator, and it provides guidelines for experiments.

The behavior of Kerr resonators can be well described by the Lugiato-Lefever equation (LLE), and a stability chart of the steady-state solutions of the LLE can provide additional insights into the behavior of Kerr resonators. For instance, the bistable range indicates the parameter space where DKSs could exist. Therefore, a modified Lugiato-Lefever equation (mLLE) that includes the SA effect in a standard LLE is deduced and used to analyze the stability chart of the proposed SA-based fiber Kerr resonator (see the derivation in Appendix A). The location of different steady-state solutions of the mLLE is plotted in Fig. 3. The area between the two red solid curves (F_-, F_+) is the bistable region where there are three equilibria corresponding to a region where DKS states may exist, while the area outside of these two curves only has one equilibrium. The bistable region of the mLLE overlaps the parameter space for the DKS obtained from numerical

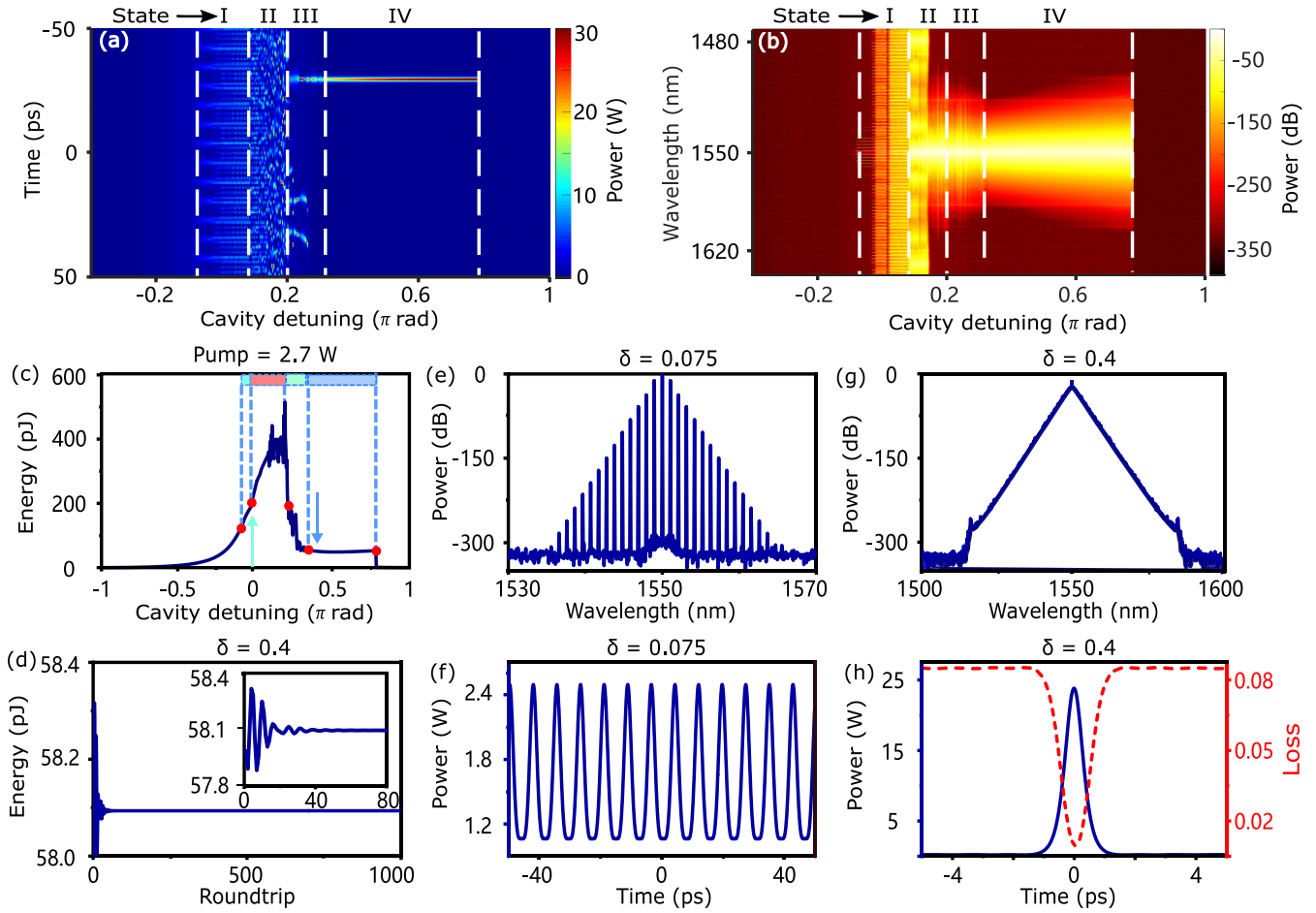

FIG. 2. Simulation results of the intracavity field evolution in SA-based fiber Kerr resonators at a pump power of 2.7 W. The SA parameters are $L_0 = 0.08$, and $P_{sat} = 10$ W. The (a) temporal and (b) spectral evolution of the intracavity field as a function of the detuning. (c) The intracavity energy upon the scan of the detuning. (d) The convergence of the energy of the intracavity field at a detuning of 0.4π rad confirms the stable soliton solution obtained in simulations. Parts (e) and (f) are the spectrum and temporal profile of the Turing roll pattern, respectively, at a detuning of 0.075π rad. Parts (g) and (h) are the spectrum and temporal profile of DKS, respectively, at a detuning of 0.4π rad.

simulations. Furthermore, the dependence of the bistable range of the mLLE on the instantaneous intracavity power is also studied and presented in Fig. 7 in Appendix B, revealing a positive relationship between the intracavity power and the bistable range. These results indicate that a stability chart based on the mLLE can serve as the first step toward selecting and optimizing the system parameters for getting a DKS in simulations.

It is well known that the final states of the DKS pattern in Kerr resonators seriously depend on initial conditions. This is the very typical behavior in externally driven, damped Kerr resonators. Therefore, the DKS region in the (Δ, F) space in Fig. 3 presents the maximum region where stable DKSs are observed in our simulations with different initial conditions.

To reflect the universality of this behavior in our SA-based system, we depict the evolution of the intracavity field in the detuning scan process for three different initial conditions in Fig. 4, revealing that the DKS step during the detuning scan is slightly different for different DKS solutions. The DKS step is a range of the detuning where one can achieve soliton states. The pump is 2.7 W and the detuning is $\delta = 0.4\pi$ rad. It can be seen that the range of the DKS step is inversely proportional to the number of DKSs, i.e., the more the DKS is excited, the smaller is the DKS step. A possible explanation of the inverse relationship between the DKS step and the number of DKSs is that the soliton properties rely significantly on the parameter of the detuning. The detuning describes the frequency offset between the pump frequency and the cavity resonance, hence determining the pump-to-soliton energy-transfer efficiency. Because the soliton states are usually obtained for a red-detuned pump, further scanning the detuning into the far red-detuned side could lower the energy transfer efficiency a lot. In this case, for multisoliton states in an anomalous dispersion regime where the pulse energy of each soliton is constrained due to the soliton area theorem, the intracavity power cannot support the multisoliton operation in the far red-detuned region. However, a single soliton can survive. Based on the theory, back-scanning the detuning to control the DKS number has been successfully implemented in the microresonators [3,16]. Figure 4(b) shows the convergence of the peak power of the intracavity field under these three initial conditions, and (c) and (d) are the temporal profile and the

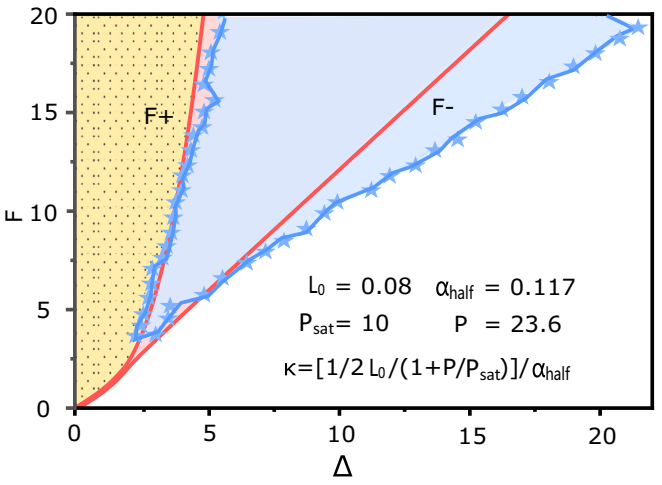

FIG. 3. Map of different solutions of the SA-based fiber Kerr resonator in a two-dimensional space of (Δ, F) (Δ is the normalized detuning and F is the normalized pump power). The modulation depth of the SA is 0.08 and its saturation power is 10 W. The half-loss of the fiber cavity is 0.117. The light yellow area (punctate area) represents the parameter space for chaotic patterns, whereas the light blue area enclosed by stars indicates the location where DKS can be excited. Note that the red solid curves $F+$ and $F-$ represent the upper and lower boundary of the bistable range of a modified LLE (mLLE) that is derived to describe the behavior of the SA-based fiber Kerr resonator. The details of the derivation of the mLLE are given in Appendix A.

spectrum profile of the final states, respectively, demonstrating the generation of different DKS states, including a single DKS, two DKSs, and three DKSs.

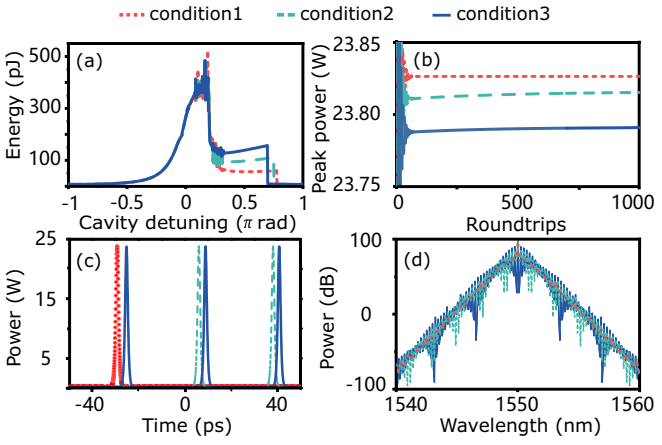

FIG. 4. The dependence of the steady-state solutions on the initial conditions in the SA-based fiber Kerr resonator. The modulation depth of the SA is 0.08 and the saturation power is 10 W. The pump power is 2.7 W and the detuning is $\delta = 0.4\pi$ rad. Simulation results of stable DKS solutions with different initial conditions. (a) The evolution of the intracavity energy as the detuning linearly scans from $-\pi$ rad to π rad. (b) The convergence of the intracavity peak power over roundtrips. (c) Temporal profile and (d) spectral intensity profile of different DKS solutions, respectively.

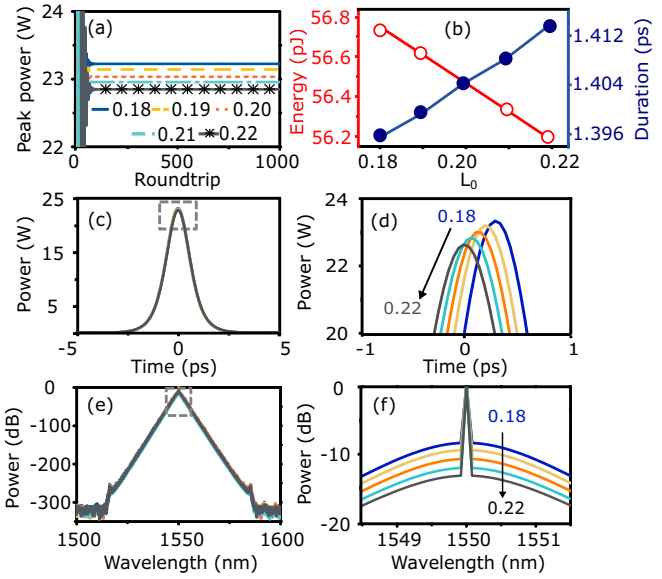

FIG. 5. The influence of the modulation depth of the SA on the DKS performances at $\delta = 0.36\pi$ rad and a pump power of 2.7 W. The modulation depth changes from 0.18 to 0.22 with a step size of 0.01. (a) The evolution of the peak power over roundtrips. (b) The pulse energy (left) and its duration (right) as a function of the modulation depth. (c) The pulse profile and (d) the corresponding spectrum profile in the case of different modulation depths.

C. The influence of the SA properties on DKS performance

In the mode-locking regime, the SA introduces a power-dependent amplitude modulation on the intracavity field and hence helps with the formation of pulse structures and also stabilizes the mode-locking operation. One could expect that the SA employed in the Kerr resonators would be beneficial to the performances of DKSs. To figure this out, we first keep all parameters constant except for the modulation depth of the SA in order to study the impact of the modulation depth of the SA on DKS performances. The detuning is 0.36π rad and the pump power is 2.7 W. The saturation power is 10 W. As shown in Fig. 5, varying the modulation depth L_0 from 0.18 to 0.22 allows the generation of DKSs. Figure 5(b) depicts the energy of the DKS and its pulse duration as a function of L_0, revealing that an increase of L_0 leads to a slight decrease in the pulse energy. Consequently, the pulse is broadened because of the soliton area theorem. Figures 5(c) and 5(d) show the pulse profile and broad spectrum of the DKS under five different values of L_0, confirming the generation of the DKS solutions and also indicating the weak influence of L_0 on DKS performances.

Furthermore, the impact of the saturation power of the SA on the performances of the DKS is also studied. In this case, the detuning is 0.36π rad and the pump power is 2.7 W. We keep the modulation depth a constant $L_0 = 0.18$ and vary the saturation power P_{sat} of the SA from 14 to 22 W. Figure 6(a) shows the evolution of the peak power of the intracavity field along with the roundtrips, demonstrating that stable solutions of DKSs can be achieved. The temporal profile and the spectrum shown in Figs. 6(c) and 2(d) further confirm the DKS solutions. The pulse duration of the DKS is

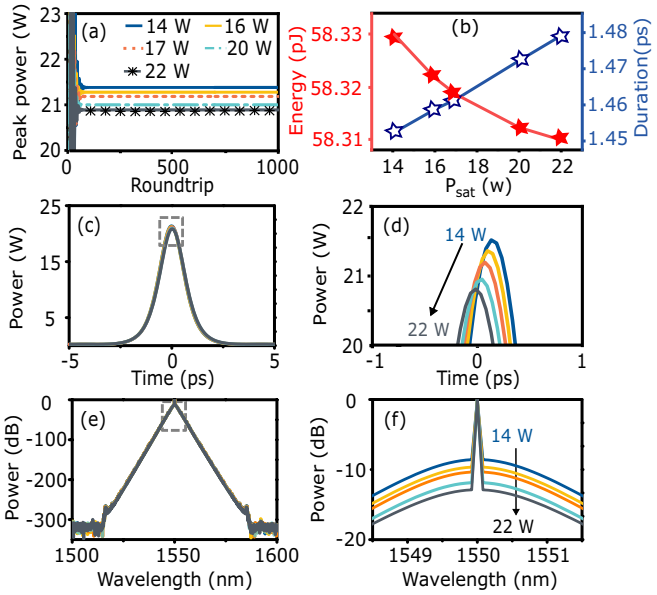

FIG. 6. The impact of the saturation power of the SA on the DKS performances at $\delta = 0.36\pi$ rad and a pump power of 2.7 W. The modulation depth L_0 is fixed at 0.18. (a) The evolution of the peak power over roundtrips. (b) The pulse energy and duration as a function of saturation power. (c) The pulse profile and (d) the spectrum profile in the case of different saturation power.

proportional to P_{sat}, whereas the pulse energy varies inversely as P_{sat} [Fig. 6(b)]. Although the simulation results also indicate a weak dependence of the DKS performance on the SA parameters, these results point out a direction for further improving the DKS performance by using an SA with a lower modulation depth and lower saturation power.

IV. DISCUSSIONS AND CONCLUSIONS

Our work demonstrates the existence of DKSs in fiber Kerr resonators with a fast SA inside the resonators. The influence of the SA parameters on the DKS performances is also studied. Although by playing with the SA parameters no significant boost in the DKS performances is observed, we believe that using a SA with a lower modulation depth and lower saturation power could improve the performances of the DKS. Most importantly, our work paves the way to implement SA-based fiber Kerr resonators in different dispersion regimes, which may improve the single pulse energy of the DKS. Furthermore, considering the role of the SA in pulse initiation and stabilization in practice as well as its advantages of a simple structure, easier integration with a fiber system, and ultrashort pulse generation, our results will drive the design of robust fiber Kerr comb systems, offering a potential way to overcome the shortage of spontaneous emission and robust operation of Kerr solitons in fiber Kerr resonators. We recognize, however, that experiments must still be conducted, which is the direction of our future work. Also, the integration of SAs like graphene or carbon nanotubes with fiber Kerr resonators may allow the realization of resonators with multifunctions, such as a tunable working wavelength and an adjustable pulse repetition rate [36].

As a complement to the numerical simulation results, we have derived in Appendix A a modified mean-field LLE (mLLE) of the SA-based fiber Kerr resonator, and we analyze the stability chart of such a system in a two-dimensional space of the pump power and detuning (see details in Appendix B), revealing that the bistable range of the mLLE is positively related to the instantaneous intracavity power. The bistable range of the mLLE overlaps the existing range of parameters for DKS excitation that is obtained in simulations, indicating that the stability chart of the system can serve as the first step toward selecting parameters and optimizing the simulations.

The implementation of the SA in fiber resonators enhances the flexibility of the Kerr resonator system. On the one hand, the parameters of the SA provide additional degrees of freedom to optimize the system performance. Indeed, a very recently published paper demonstrates the controllable generation of soliton crystal in microresonators benefiting from the active role of the SA in the cavity [37]. The SA enables the system to form a desired soliton crystal state directly from the previous Turing pattern without passing the chaotic states. Hence, the number of pulses in the soliton crystal can be fully designed by changing the pump power and SA parameters. Unlike the difficulty of integrating an SA in microresonators, it is much easier and more practical to construct a fiber Kerr resonator with an SA in the cavity.

On the other hand, our work on the existence of DKSs in fiber Kerr resonators with an SA inside the cavity in anomalous dispersion regimes may stimulate an enormous amount of research on SA-based Kerr resonators in normal dispersion regimes. The current performances of Kerr solitons from micro/fiber Kerr resonators are poor in terms of pulse energy and average power, due to the low pump-to-soliton energy transfer efficiency and soliton area theorem in the anomalous dispersion regime. A major research avenue in this field is to explore the potential of DKSs in normal dispersion regimes. However, a Kerr resonator in the normal dispersion regime will suffer from difficulties in initiating the soliton state in the resonators, because the threshold for DKS excitation in such resonators is comparably higher. In this respect, our work may point out a direction for solving the difficulty of getting DKSs in a normal dispersion Kerr resonator by putting an SA inside the resonator. The SA-based fiber resonators in different dispersion regimes, including zero-dispersion or normal-dispersion regimes, may allow the generation of dispersion-managed DKSs with higher pulse energy, which arouses our further interest.

Finally, the transient loss modulation on the intracavity field in micro-Kerr resonators has been proven instrumental to the self-starting, robustness, and stability of DKS operation [34,35]. Therefore, we can also imagine that the noise feature, the robustness, and the stabilities of the DKS excited in SA-based fiber Kerr resonators are improved but need experimental evidence. Incidentally, a fiber Kerr resonator that is typically emitting pulses at a low repetition rate of MHz enables us to implement real-time time-frequency measurements. A robust system of fiber Kerr resonators with SA inside the cavity hence provides a good testbed to explore the behavior of the nonlinear Kerr system, hence it will shed more light on the DKS dynamics in Kerr resonators.

APPENDIX A: A MODIFIED LUGIATO-LEFEVER EQUATION AND THE STABILITY CHART ANALYSIS

We analytically analyze the bistable area of the system of an SA-based fiber Kerr resonator using the mLLE where an additional term describing the extra nonlinear loss introduced by the fast SA is included. Compared to the prior studies, our model considers the saturation effect of the SA in the Kerr resonator system, hence providing additional insight into the behavior of the fiber Kerr resonators with the SA in the resonators. The mLLE is shown as follows:

$$T_R\frac{\partial E(t,\tau)}{\partial t}=\sqrt{\theta}E_{\rm in}+\left[-\alpha_{\rm SA}(t,\tau)-\alpha-i\delta_0 - iL\frac{\beta_2}{2}\frac{\partial^2}{\partial\tau^2}+i\gamma L|E|^2\right]E, \quad \text{(A1)}$$

where T_R is the roundtrip time, t is the fast time, α is half of the total cavity loss, and the additional term $\alpha_{\rm SA}(t,\tau)$ is half of the loss provided by the fast SA. We use the following transformations:

$$t'\to t\frac{\alpha}{T_R},\quad \tau'\to\tau\sqrt{\frac{2\alpha}{|\beta_2|L}},\quad E'\to E\sqrt{\frac{\gamma L}{\alpha}},$$
$$\kappa(\tau')=\frac{\alpha_{\rm SA}(t',\tau')}{\alpha},\quad \Delta=\frac{\delta_0}{\alpha},\quad D_{\rm in}=\sqrt{\frac{\theta\gamma L}{\alpha^3}}E_{\rm in}. \quad \text{(A2)}$$

Equation (A1) can be normalized to a dimensionless two-parameter model, which can be characterized as in the panel corresponding with the laser detuning and the pump power,

$$\frac{\partial E'}{\partial t'}=D_{\rm in}+\left[-\kappa(\tau')-1-i\Delta-i\,\mathrm{sgn}(\beta_2)\frac{\partial^2}{\partial\tau'^2}+i|E'|^2\right]E'. \quad \text{(A3)}$$

For the steady-state solutions (CW solutions), the derivative terms in Eq. (A3) should equal zero, namely $\frac{\partial E'}{\partial t'}=0$ and $\frac{\partial^2 E'}{\partial\tau'^2}=0$. Then we can obtain

$$D_{\rm in}=[[\kappa(\tau')+1]-i(|E'|^2-\Delta)]E'. \quad \text{(A4)}$$

To find the steady-state solutions, the fast time-dependent characteristic of the SA is ignored from hereon, and hence $\kappa(\tau)$ is reduced to

$$\kappa(\tau')=\kappa=\frac{1}{2\alpha}\frac{L_0}{1+P/P_{\rm sat}}, \quad \text{(A5)}$$

where P is a constant representing the instantaneous power of the intracavity field. Taking the square modular of both sides in Eq. (A4), we obtain the following relationships among pump power, cavity loss, detuning, and intracavity power:

$$F=\rho[(\kappa+1)^2+(\rho-\Delta)^2], \quad \text{(A6)}$$

where $F=|D_{\rm in}|^2$ is the pump power, and $\rho=|E'|^2$ is the transient intracavity power. Equation (A6) is a cubic polynomial equation in ρ. To make it clear, we rewrite Eq. (A6) as follows:

$$F=\rho^3-2\rho^2\Delta+\Delta^2\rho+(\kappa+1)^2\rho. \quad \text{(A7)}$$

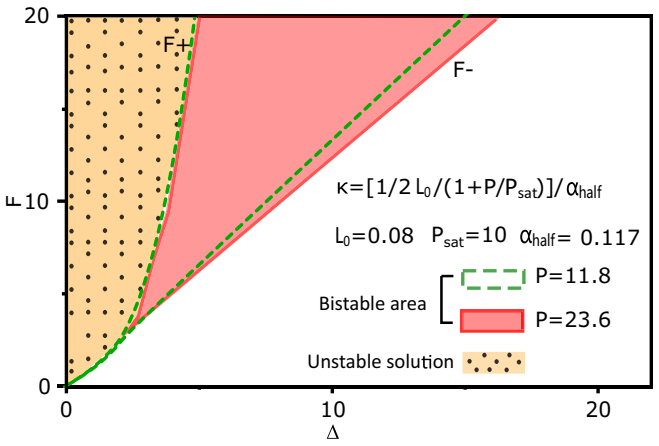

FIG. 7. Bifurcation diagram to scale, showing the bistable area of DKS solutions of the mLLE in two cases of $P=11.8$ and 23.6, respectively.

The solutions to Eq. (A7) are dependent on the parameters Δ and F. The number of solutions is either one, two, or three [38]. The steady-state solution may arise in a polynomial equation when it has local extrema and hence requires the existence of critical ρ satisfying the following equation [22]:

$$3\rho^2-4\Delta\rho+\Delta^2+(\kappa+1)^2=0. \quad \text{(A8)}$$

This is a quadratic equation, and the discriminant is $\sqrt{\Delta^2-3(\kappa+1)^2}$. Therefore, when $\Delta\geqslant\sqrt{3}(\kappa+1)$, the critical solutions are

$$\rho_\pm=\frac{2\Delta\pm\sqrt{\Delta^2-3(\kappa+1)^2}}{3}. \quad \text{(A9)}$$

Therefore, the corresponding pump power can be obtained:

$$F_\pm=\frac{2\Delta\mp\sqrt{\Delta^2-3(\kappa+1)^2}}{3}\times\left[(\kappa+1)^2+\left(\frac{\sqrt{\Delta^2-3(\kappa+1)^2}\pm\Delta}{3}\right)^2\right]. \quad \text{(A10)}$$

When $\Delta\geqslant\sqrt{3}(\kappa+1)$, three equilibria (ρ_1,ρ_2,ρ_3) can be found in the range $F(\Delta)\in[F_-(\Delta),F_+(\Delta)]$, where $\rho_1\leqslant\rho_-\leqslant\rho_2\leqslant\rho_+\leqslant\rho_3$. Therefore, the extrema solutions ρ_1 and ρ_3 are always stable, while the intermediate solution ρ_2 is unstable. Outside of this range, there is only one unique equilibrium. Therefore, we can estimate the existing range of DKS solutions by plotting the stability chart. The DKS usually forms within the bistable region, namely within the pump range $[F_-(\Delta),F_+(\Delta)]$.

APPENDIX B: THE DEPENDENCE OF THE BISTABLE AREA OF THE mLLE ON THE INSTANTANEOUS INTRACAVITY POWER

To investigate how the instantaneous intracavity power influences the bistable range of the SA-based fiber Kerr resonator, we show in Fig. 7 the stability chart of the mLLE in the panel $(\Delta-F)$ for different instantaneous intracavity power when $\rho\neq1$. The SA parameters are $\alpha_{\rm half}=0.117$, $L_0=0.08$,

and $P_{sat} = 10$ W. As stated in Appendix A, the fast-time-dependent characteristic of the SA is ignored for simplicity, and the term $P = |E(z, \tau)|^2$ is assumed to be a constant that is varying accordingly. The normalized detuning Δ is varying from 0 to 20, and the normalized pump power F is in the range from 0 to 20. The area within the triangular green dash-dotted lines is the bistable area corresponding to a case of $P = 11.8$, and the area within the triangular pink solid lines is for the case of $P = 23.6$. The yellow area (punctate area) outside of the $[F_-, F_+]$ range corresponds to the unstable solutions. It can be seen that the saturation degree of the SA has a positive impact on the bistable area. For a larger value P of 23.6, the bistable range is wider, while when P decreases to 11.8, the bistable range shrinks. Note that the fast time-dependent property of the SA has been ignored in the aforementioned analysis, hence the colored region in Fig. 7 is not strictly the parameter space where the bistable solutions exist. Detailed numerical simulations based on a lumped model need to be conducted. However, studying the dependence of the bistable range of the system on the parameter of P reveals the positive relationship between the instantaneous power and the soliton existence range, which guides the selection of parameters in numerical simulations.

APPENDIX C: COMPARISON OF NUMERICAL SIMULATION RESULTS OF THE IKEDA MAP FOR FIBER KERR RESONATORS WITH/WITHOUT AN SA

We admit that the insertion of the SA in fiber Kerr resonators reduces the existence range of the DKS solutions when compared with a fiber Kerr resonator without an SA. A comparison of numerical simulation results of the Ikeda map for fiber Kerr resonators with and without an SA is shown in Fig. 8. The area between the black dotted line is the parameter space on the (Δ, P) plane for DKSs in the case of fiber Kerr resonator with an SA, while the area within the two white dashed lines is for the case of a pure fiber Kerr resonator without an SA. The color represents the intensity of the intracavity field. Consequently, different colors correspond to different solutions. For instance, the red area represents the unstable MI pattern. The uniform light blue corresponds to the breathing DKSs and stable DKS solutions, while the dark blue is the CW solution. This comparison demonstrates that the SA narrows down the parameter space for the DKS to survive in the fiber Kerr resonators due to the additional loss introduced by the SA. However, we remind ourselves that in this article we focus on exploring the existence of DKSs in SA-based fiber Kerr resonators, paving the way to construct such systems in practice, which, on the one hand, enables the spontaneous generation and stable operation of DKSs in fiber Kerr resonators without external perturbations, and on the other hand demonstrates the feasibility of SA-based fiber Kerr resonators operating in dispersion-managed regimes.

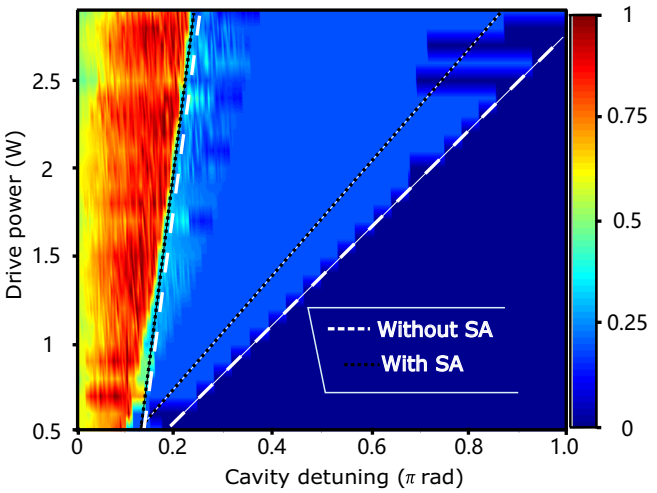

FIG. 8. The map of different solutions in a two-dimensional plane (the detuning and pump power) for a fiber Kerr resonator with and without an SA. The modulation depth of the SA is 0.08 and the saturation power is 10 W.

[1] F. Leo, S. Coen, P. Kockaert, S.-P. Gorza, P. Emplit, and M. Haelterman, Temporal cavity solitons in one-dimensional kerr media as bits in an all-optical buffer, Nat. Photon. **4**, 471 (2010).

[2] T. J. Kippenberg, R. Holzwarth, and S. A. Diddams, Microresonator-based optical frequency combs, Science **332**, 555 (2011).

[3] T. Herr, V. Brasch, J. D. Jost, C. Y. Wang, N. M. Kondratiev, M. L. Gorodetsky, and T. J. Kippenberg, Temporal solitons in optical microresonators, Nat. Photon. **8**, 145 (2014).

[4] P. Marin-Palomo, J. N. Kemal, M. Karpov, A. Kordts, J. Pfeifle, M. H. Pfeiffer, P. Trocha, S. Wolf, V. Brasch, M. H. Anderson, *et al.*, Microresonator-based solitons for massively parallel coherent optical communications, Nature (London) **546**, 274 (2017).

[5] D. T. Spencer *et al.*, An optical-frequency synthesizer using integrated photonics, Nature (London) **557**, 81 (2018).

[6] S. B. Papp, K. Beha, P. Del'Haye, F. Quinlan, H. Lee, K. J. Vahala, and S. A. Diddams, Microresonator frequency comb optical clock, Optica **1**, 10 (2014).

[7] J. Riemensberger, A. Lukashchuk, M. Karpov, W. Weng, E. Lucas, J. Liu, and T. J. Kippenberg, Massively parallel coherent laser ranging using a soliton microcomb, Nature (London) **581**, 164 (2020).

[8] A. Dutt, C. Joshi, X. Ji, J. Cardenas, Y. Okawachi, K. Luke, A. L. Gaeta, and M. Lipson, On-chip dual-comb source for spectroscopy, Sci. Adv. **4**, e1701858 (2018).

[9] T. M. Fortier, M. S. Kirchner, F. Quinlan, J. Taylor, J. Bergquist, T. Rosenband, N. Lemke, A. Ludlow, Y. Jiang, C. Oates *et al.*, Generation of ultrastable microwaves via optical frequency division, Nat. Photon. **5**, 425 (2011).

[10] P. Del'Haye, A. Schliesser, O. Arcizet, T. Wilken, R. Holzwarth, and T. J. Kippenberg, Optical frequency comb generation from a monolithic microresonator, Nature (London) **450**, 1214 (2007).

[11] H. Bao, L. Olivieri, M. Rowley, S. T. Chu, B. E. Little, R. Morandotti, D. J. Moss, J. S. Totero Gongora, M. Peccianti, and A. Pasquazi, Turing patterns in a fiber laser with a nested

microresonator: Robust and controllable microcomb generation, Phys. Rev. Res. **2**, 023395 (2020).

[12] A. B. Matsko, A. A. Savchenkov, D. Strekalov, V. S. Ilchenko, and L. Maleki, Optical hyperparametric oscillations in a whispering-gallery-mode resonator: Threshold and phase diffusion, Phys. Rev. A **71**, 033804 (2005).

[13] C. Joshi, J. K. Jang, K. Luke, X. Ji, S. A. Miller, A. Klenner, Y. Okawachi, M. Lipson, and A. L. Gaeta, Thermally controlled comb generation and soliton modelocking in microresonators, Opt. Lett. **41**, 2565 (2016).

[14] T. Carmon, L. Yang, and K. J. Vahala, Dynamical thermal behavior and thermal self-stability of microcavities, Opt. Express **12**, 4742 (2004).

[15] T. Herr, K. Hartinger, J. Riemensberger, C. Wang, E. Gavartin, R. Holzwarth, M. Gorodetsky, and T. Kippenberg, Universal formation dynamics and noise of kerr-frequency combs in microresonators, Nat. Photon. **6**, 480 (2012).

[16] H. Guo, M. Karpov, E. Lucas, A. Kordts, M. H. Pfeiffer, V. Brasch, G. Lihachev, V. E. Lobanov, M. L. Gorodetsky, and T. J. Kippenberg, Universal dynamics and deterministic switching of dissipative kerr solitons in optical microresonators, Nat. Phys. **13**, 94 (2017).

[17] V. Brasch, M. Geiselmann, M. H. Pfeiffer, and T. J. Kippenberg, Bringing short-lived dissipative kerr soliton states in microresonators into a steady state, Opt. Express **24**, 29312 (2016).

[18] H. Zhou, Y. Geng, W. Cui, S.-W. Huang, Q. Zhou, K. Qiu, and C. Wei Wong, Soliton bursts and deterministic dissipative kerr soliton generation in auxiliary-assisted microcavities, Light Sci. Appl. **8**, 1 (2019).

[19] X. Xue, Y. Xuan, Y. Liu, P.-H. Wang, S. Chen, J. Wang, D. E. Leaird, M. Qi, and A. M. Weiner, Mode-locked dark pulse kerr combs in normal-dispersion microresonators, Nat. Photon. **9**, 594 (2015).

[20] X. Xue, P.-H. Wang, Y. Xuan, M. Qi, and A. M. Weiner, Microresonator kerr frequency combs with high conversion efficiency, Laser Photon. Rev. **11**, 1600276 (2017).

[21] A. Matsko, A. Savchenkov, and L. Maleki, Normal group-velocity dispersion kerr frequency comb, Opt. Lett. **37**, 43 (2012).

[22] C. Godey, I. V. Balakireva, A. Coillet, and Y. K. Chembo, Stability analysis of the spatiotemporal lugiato-lefever model for kerr optical frequency combs in the anomalous and normal dispersion regimes, Phys. Rev. A **89**, 063814 (2014).

[23] E. Obrzud, S. Lecomte, and T. Herr, Temporal solitons in microresonators driven by optical pulses, Nat. Photon. **11**, 600 (2017).

[24] M. Anderson, Y. Wang, F. Leo, S. Coen, M. Erkintalo, and S. G. Murdoch, Coexistence of Multiple Nonlinear States in a Tristable Passive Kerr Resonator, Phys. Rev. X **7**, 031031 (2017).

[25] X. Xue, X. Zheng, and B. Zhou, Super-efficient temporal solitons in mutually coupled optical cavities, Nat. Photon. **13**, 616 (2019).

[26] X. Dong, Q. Yang, C. Spiess, V. G. Bucklew, and W. H. Renninger, Stretched-Pulse Soliton Kerr Resonators, Phys. Rev. Lett. **125**, 033902 (2020).

[27] X. Dong, C. Spiess, V. G. Bucklew, and W. H. Renninger, Chirped-pulsed kerr solitons in the lugiato-lefever equation with spectral filtering, Phys. Rev. Res. **3**, 033252 (2021).

[28] N. Englebert, C. Mas Arabí, P. Parra-Rivas, S.-P. Gorza, and F. Leo, Temporal solitons in a coherently driven active resonator, Nat. Photon. **15**, 536 (2021).

[29] M. J. Ablowitz, T. P. Horikis, and B. Ilan, Solitons in dispersion-managed mode-locked lasers, Phys. Rev. A **77**, 033814 (2008).

[30] P. Grelu and N. Akhmediev, Dissipative solitons for mode-locked lasers, Nat. Photon. **6**, 84 (2012).

[31] J. K. Jang, M. Erkintalo, S. G. Murdoch, and S. Coen, Writing and erasing of temporal cavity solitons by direct phase modulation of the cavity driving field, Opt. Lett. **40**, 4755 (2015).

[32] I. Hendry, W. Chen, Y. Wang, B. Garbin, J. Javaloyes, G. L. Oppo, S. Coen, S. G. Murdoch, and M. Erkintalo, Spontaneous symmetry breaking and trapping of temporal kerr cavity solitons by pulsed or amplitude-modulated driving fields, Phys. Rev. A **97**, 053834 (2018).

[33] F. Leo, L. Gelens, P. Emplit, M. Haelterman, and S. Coen, Dynamics of one-dimensional kerr cavity solitons, Opt. Express **21**, 9180 (2013).

[34] Z. Xiao, K. Wu, T. Li, and J. Chen, Deterministic single-soliton generation in a graphene-fp microresonator, Opt. Express **28**, 14933 (2020).

[35] Y. Chen, T. Liu, S. Sun, and H. Guo, Temporal dissipative structures in optical kerr resonators with transient loss fluctuation, Opt. Express **29**, 35776 (2021).

[36] B. Yao, S.-W. Huang, Y. Liu, A. K. Vinod, C. Choi, M. Hoff, Y. Li, M. Yu, Z. Feng, D.-L. Kwong *et al.*, Gate-tunable frequency combs in graphene–nitride microresonators, Nature (London) **558**, 410 (2018).

[37] A. Nakashima, S. Fujii, R. Imamura, K. Nagashima, and T. Tanabe, Deterministic generation of a perfect soliton crystal microcomb with a saturable absorber, Opt. Lett. **47**, 1458 (2022).

[38] I. V. Barashenkov and Y. S. Smirnov, Existence and stability chart for the ac-driven, damped nonlinear schrödinger solitons, Phys. Rev. E **54**, 5707 (1996).